DETERMINING OF GEOMETRICAL CHARACTERISTIC PARAMETERS OF PARTICLE FRACTAL AGGREGATES FROM LIGHT SCATTERING MEASUREMENT SIGNALS

by

Liang XU, Zhen-Zong HE**, Jun-Kui MAO, and Xing-Si HAN

Jiangsu Province Key Laboratory of Aerospace Power System,
College of Energy and Power Engineering,
Nanjing University of Aeronautics and Astronautics, Nanjing, China

Original scientific paper
https://doi.org/10.2298/TSCI200214203X

Two kind of light scattering measurement methods, i.e. the forward light scattering measurement method and the angular light scattering measurement method, are applied to reconstruct the geometrical morphology of particle fractal aggregates. An improved attractive and repulsive particle swarm optimization algorithm is applied to reconstruct the geometrical structure of fractal aggregates. It has been confirmed to show better convergence properties than the original particle swarm optimization algorithm and the attractive and repulsive particle swarm optimization algorithm. Compared with the forward light scattering measurement method, the angular light scattering measurement method can obtain more accurate and robust results as the distribution of the fitness function value obtained by the angular light scattering measurement method is more satisfactory. Meanwhile, the retrieval accuracy can be improved by increasing the number of measurement angles or the interval between adjacent measurement angles even when the random noises are added. All the conclusions have important guiding significance for the further study of the geometry reconstruction experiment of fractal aggregates.

Key words: *light scattering measurement method, geometrical morphology, particle fractal aggregate, inverse radiation problem*

Introduction

Particles, such as soot, aerosol and ash, *etc*., usually suspend in the atmosphere or other industrial equipment, *e.g*. combustors and furnaces, in the form of fractal aggregation. In the study of radiative heat transfer in the industrial equipment and the light radiation transmission in the atmosphere, the particles' absorption and scattering properties, depended on morphology, particle size distribution and the complex refractive index, usually play an important role according to the radiative heat transfer theory and the Maxwell scattering theory [1, 2]. The complex refractive index describes the particle's interactions with radiation and its optical properties. The complex refractive index and the particle size distribution are particle's fundamental properties. They are considered unchanged by sampling. Many scholars have carried out different studies on them using several types of methods and obtained many instructive results. The morphology of the particle and its aggregation is a non-essential attribute and easily changed in the factual industrial process, which also has an significant impact on studying the

* Corresponding author, e-mail: hezhenzong@nuaa.edu.cn

radiative properties of particles [3, 4], Moreover, the morphology of the particle aggregate is usually changing transiently in the atmosphere or other industrial equipment, which increases the complexity and difficulty of reconstructing the morphology of particle aggregates.

In order to obtain the geometric morphology of the particle aggregates, various measurement methods are developed. There are two types of measurements, classified as intrusive or not. In terms of the intrusive measurement methods, the geometric parameters, used to describe the geometric morphology of the particle aggregates, can be obtained directly by sampling, observing using TEM or SEM, rebuild the 3-D structure using image matching technique, and describing using the fractal aggregation theory [5, 6]. However, there are also several defects in using the intrusive measurement methods, such as the morphology of the particle aggregates easily disturbed and damaged by sampling, large enough sample required to ensure the generality of the results, and online monitoring unavailable [7]. The non-intrusive measurement methods are proposed to overcome these difficulties and obtain more accurate results. The morphology of the particle aggregates can be estimated from the external radiative transmission signals of the particle dispersed medium using the radiative inverse problem. For the light radiative transmission signals provide a wealth of measurement information related to the spectrum, angle and position, the morphology of particle aggregates is estimated by many optical measurement methods [7-10]. However, it is still a challenging problem to accurately predict the geometrical morphology of the particle aggregates, which needs further study.

In the present work, two kind of light scattering measurement methods, *i.e.* the forward light scattering measurement (FLSM) method and the angular light scattering measurement (ALSM) method are used to reconstruct particle fractal aggregates' geometric morphology. The retrieval accuracies are compared. In addition, the influence of obtaining measurement signals from different measurement angles on the accuracy of prediction results is also studied. An improved attractive and repulsive particle swarm optimization (IARPSO) algorithm is applied to retrieve relevant parameters. The main contents are as follows. First of all, the principles of the fractal aggregate theory, the light scattering measurement method and the inverse algorithms are described. After that, the FLSM and ALSM methods using different measurement angles are applied to reconstruct the fractal aggregates' geometrical structure. Finally, the prospects for further research and the main conclusions are discussed.

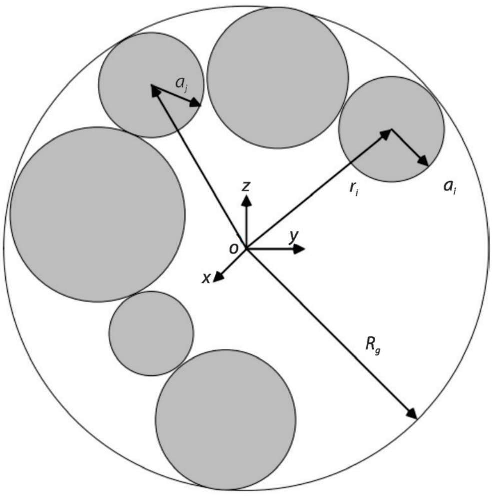

Figure 1. Schematic of fractal-like aggregates

The direct problem

The fractal aggregate theory

It can be seen from fig. 1 that the geometrical characteristic parameters play an important role in describing the morphology and construction of the particle aggregate. The corresponding formulas [11]:

$$N_{\mathrm{p}} = k_{\mathrm{f}} \left(\frac{R_{\mathrm{g}}}{a} \right)^{D_{\mathrm{f}}} \tag{1}$$

$$R_g^2 = \frac{1}{N_p}\sum_{i=1}^{N_s} r_i^2 \tag{2}$$

where r_i is the distance from the i^{th} sphere to the center of the aggregate mass and R_g – the root mean square radius. It is assumed to obey the log-normal (L-N) distribution, and can be expressed:

$$f_{\text{L-N}}(R_g) = \frac{1}{\sqrt{2\pi}R_g \ln\sigma}\exp\left[-\frac{\left(\ln R_g - \ln R_{g,av}\right)^2}{2\left(\ln\sigma\right)^2}\right] \tag{3}$$

where $R_{g,av}$ and σ are the mean and variance, respectively.

The radiative properties of fractal aggregates with diverse geometric morphologies have been studied in our previous work [4], and the results revealed that the fractal prefactor has little effect on the soot aggregates' radiative characteristics. Thus, the primary particle's total number, N_p, and the mean radius are considered as known parameters to simplify calculations in this paper, *i.e.* $N_p = 20$, $a = 15$ nm, and the present manuscript mainly investigates R_g and D_f.

The light scattering measurement methods

The particle dispersion medium filled with fractal aggregates of absorbing and scattering particles is impacted by a collimated monochromatic laser beam at room temperature. When the medium emission is not considered, the transmission of light in the medium can be described by the 1-D steady-state radiative transfer equation. The mathematical expression [1]:

$$\vec{s}\frac{\partial I_\lambda(z,\vec{s})}{\partial z} = -(\alpha_\lambda + \sigma_\lambda)I_\lambda(z,\vec{s}) + \frac{\sigma_\lambda}{4\pi}\int_{4\pi} I_\lambda(z,\vec{s}_i)\Phi_\lambda(\vec{s}_i,\vec{s})\mathrm{d}\Omega_i \tag{4}$$

where λ is the wavelength of incident laser, $I_\lambda(z, \vec{s})$ – the spectral radiative intensity in direction $\vec{s}$ at location z, σ_λ – the spectral scattering coefficient, α_λ – the spectral absorption coefficient, $\Phi_\lambda(\vec{s}_i, \vec{s})$ – the scattering phase function, and Ω_i – the solid angle. The mathematical expressions of α_λ, σ_λ, and $\Phi_\lambda(\vec{s}_i, \vec{s})$:

$$\alpha_\lambda = \sum_{i=1}^{n} N(R_{g,i})C_{\text{abs},\lambda,i}^{agg} \tag{5}$$

$$\sigma\lambda = \sum_{i=1}^{n} N(R_{g,i})C_{\text{sca},\lambda,i}^{agg} \tag{6}$$

$$\Phi_\lambda(\vec{s}_i,\vec{s}) = \frac{1}{\sigma_\lambda}\sum_{i=1}^{n} N(R_{g,i})C_{\text{sca},\lambda,i}^{agg}\Phi_{p,i}(\vec{s}_i,\vec{s}) \tag{7}$$

where $N(R_{g,i})$ is the sample's number concentration, $N(R_{g,i}) = N_{tot}\times f_{\text{L-N}}(R_{g,i})$, N_{tot} – the sample's total number concentration, a prior information in the present study. According to Rayleigh-Debye-Gans fractal aggregate method [9], $C_{\text{abs},\lambda,i}^{agg}$, $C_{\text{sca},\lambda,i}^{agg}$, and $\Phi_{p,i}$ are the absorption cross-section, scattering cross-section and scattering phase function of fractal aggregates, respectively. They are available in [11].

The boundary conditions can be expressed as follows when solving the 1-D steady-state radiative transfer equation:

$$I_\lambda^+(0,\theta) = \begin{cases} I_0, & \theta = 0 \\ 0, & 0 < \theta \le \dfrac{\pi}{2} \end{cases} \tag{8}$$

$$I_\lambda^-(L,\theta)=0,\ \frac{\pi}{2}<\theta<\pi \tag{9}$$

where I_0 is the total incident light intensity, $I_\lambda^+(0,\theta)$ and $I_\lambda^-(0,\theta)$ are the light intensity incident to the internal medium from the light incident side and light output side of the sample, respectively.

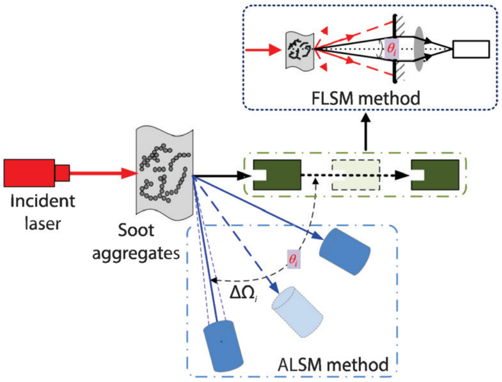

Figure 2. Schematic model of LSM methods

In order to investigate the geometrical structure of the particle fractal aggregates, two kind of light scattering measurement methods, *i.e.* the FLSM method and the ALSM method, are proposed. The schematic models of both methods are depicted in fig. 2. For the ALSM method, the mathematical formula of the corresponding measurement signals $I_a(\theta_i)$ at measurement angle θ_i within corresponding solid angle $\Delta\Omega_i$ can be expressed:

$$I_a(\theta_i)=I_\lambda^+(L,\theta_i)\Delta\Omega_i,\ \theta_i\in[0,90^\circ] \tag{10}$$

For the FLSM method, the corresponding measurement signals $I_\mathrm{f}(\theta_i)$ within an acceptance angle θ_i can be expressed:

$$\begin{gathered}I_\mathrm{f}(\theta_i)=2\pi\int_0^{\theta_i}I(L,\theta)\cos\theta\sin\theta\mathrm{d}\theta+I_\mathrm{c}(L,0)\\ I_c(L,0)=I_0\exp\left[-(\alpha_\lambda+\sigma_\lambda)L\right],\ \theta_i\in[0,90^\circ]\end{gathered} \tag{11}$$

where $I_\mathrm{c}(L,0)$ is the intensity of the collimated light, which can be obtained by the Beer-Lambert law.

The inverse problem model

The particle swarm optimization algorithm

From the particle swarm optimization (PSO) algorithm, the mathematical expression of the velocity-update and the position-update:

$$\mathbf{V}_i(t+1)=\omega\mathbf{V}_i(t)+C_1\mathrm{rand}_1\left[\mathbf{P}_i(t)-\mathbf{X}_i(t)\right]+C_2\mathrm{rand}_2\left[\mathbf{P}_\mathrm{g}(t)-\mathbf{X}_i(t)\right] \tag{12}$$

$$\mathbf{X}_i(t+1)=\mathbf{X}_i(t)+\mathbf{V}_i(t+1) \tag{13}$$

The detail of PSO algorithm is available in [12].

The attractive and repulsive particle swarm optimization algorithm

Despite the aforementioned advantages, the PSO algorithm is difficult to avoid local optimization with the rapid decline of diversity, which will lead to low diversity, and the overall result is the stagnation of fitness. In order to overcome these difficulties, the attractive and repulsive particle swarm optimization algorithm (ARPSO) algorithm was introduced [13], which avoids premature convergence. Premature convergence is one of the main problems of the evolutionary algorithm in multi-modal optimization. It leads to suboptimal solution and performance loss. The attraction phase is defined merely as the PSO algorithm in the ARPSO algorithm. The reason is that there is information flow of good solutions between particles, and particles would attract each other in the basic PSO algorithm. The second phase repulsion is also defined by *inverting* the velocity-update formula of the particles. In this way, velocity-update can be expressed [14]:

$$\mathbf{V}_i(t+1)=\omega\mathbf{V}_i(t)+\mathrm{dir}\left\{C_1\left[\mathbf{P}_i(t)-\mathbf{X}_i(t)\right]+C_2\left[\mathbf{P}_\mathrm{g}(t)-\mathbf{X}_i(t)\right]\right\} \tag{14}$$

$$\mathbf{X}_i(t+1)=\mathbf{X}_i(t)+\mathbf{V}_i(t+1) \tag{15}$$

According to the diversity-measure, the diversity of the swarm (in the pseudo-code stored in the variable *diversity*) can be expressed:

$$\mathrm{diversity}(N_\mathrm{s})=\frac{1}{|N_\mathrm{s}||L_0|}\sum_{i=1}^{|N_\mathrm{s}|}\sqrt{\sum_{j=1}^{N_\mathrm{p}}\left(x_{ij}-\overline{x_j}\right)^2} \tag{16}$$

where parameter ω is the inertia weight, when calculating the new velocity $\mathbf{V}_i(t+1)$, it is used to control the magnitude of the old velocity $\mathbf{V}_i(t)$, $|N_\mathrm{s}|$ – the swarm size, $|L_0|$ – the length of the longest diagonal in the search space, N_p – the dimensionality of the problem, x_{ij} – the j^th value of the ith particle, $\overline{x}_j$ – the j^th value of the average point $\overline{x}$. The details of the ARPSO and the parameters used in this study are available in [13, 14].

The improve attractive and repulsive particle swarm optimization algorithm

Riget's research shows that ARPSO algorithm has great advantages in avoiding local optimum and improving inversion accuracy [13]. However, the diversity function proposed by Riget and Vesterstrom [13] has some disadvantages. Instead of considering the diversity of each dimension separately, the diversity of the population is obtained by comprehensively calculating the *N*-dimension, which will cause mutual influence among the dimensions and even misguide the *diffusion* and *shrinkage* movements of the algorithm. These phenomena will eventually result in different efficiencies of the algorithm between high dimensional and low dimensional cases.

In this study, to use the diversity to guide the evolution of the particle population more effectively, an improved ARPSO algorithm is proposed. In the improved ARPSO algorithm, the chaotic position is initialized by a typical logistic mapping and the diversity and inverse accuracy are improved by using the differential evolution algorithm. The chaos theory is applied as the initial conditions have a great influence on the behavior of the dynamic system. The Chaos signal is generated by using the typical logistic mapping which can be expressed [15]:

$$\begin{cases} r(0)=\mathrm{rand}_3 \\ r(k+1)=\mu r(k)\left[1-r(k)\right], \quad k=0,1,\cdots,N_\mathrm{c}-1 \end{cases} \tag{17}$$

where rand_3 is the uniformly distributed random number in the range of [0, 1], μ – the control number, when $\mu = 4.0$, the logistic mapping is in a fully chaotic state. Moreover, the personal best position is improved by using the differential evolution algorithm. The mutant vector can be derived [15, 16]:

$$\mathbf{P}_{i,\mathrm{mut}}(t)=\mathbf{P}_k(t)+F\left[\mathbf{P}_j(t)-\mathbf{P}_m(t)\right] \tag{18}$$

where k, l, and m are the random integers uniformly selected from [1, N_s] and $i \neq k \neq l \neq m$, F – the mutant factor which is considered unchanged, $F \in [0, 2]$. The amplification of the differential variation $[\mathbf{P}_j(t) - \mathbf{P}_m(t)]$ is controlled by it. The diversity of the perturbed parameter vectors is improved by applying the crossover, and the trial vector $\mathbf{P}_{i,\mathrm{tri}}(t) = (p_{i1,\mathrm{tri}}, p_{i2,\mathrm{tri}}, p_{i3,\mathrm{tri}}\ldots, pi_{N_\mathrm{p},\mathrm{tri}})$ can be derived from [15, 16]:

$$p_{ij,\mathrm{tri}}(t)=\begin{cases} p_{ij,\mathrm{mut}}(t) \ \text{ if } \ \mathrm{rand}_4(j)\le C_R \ \text{ or } \ j=rnbr(i) \\ p_{ij}(t) \ \text{ if } \ \mathrm{rand}_4(j)\le C_R \ \text{ or } \ j\neq rnbr(i) \end{cases} \tag{19}$$

where $\text{rand}_4(j)$ is the j^{th} evaluation of a uniform random number generator, $\text{rand}_4(j) \in [0, 1]$, C_R – the crossover constant $C_R \in [0, 1]$. The value of it is initialized by the user, $\text{rnbr}(i)$ – the random integer uniformly selected from $[1, N_s]$. The flow of the improve attractive and repulsive particle swarm optimization algorithm (IARPSO) is as follows.

Step 1. Assign initial values to system control parameters, *i.e.* the total number of the particles in the swarm N_s, the maximum number of iterations N_c, the number of the inversion parameters (dimensions) N_n, the searching space $[\text{low}_i, \text{high}_i]$ of each inversion parameter, the tolerance for minimizing the fitness function value ε and the values of C_1, C_2, F, d_{low}, d_{high}, and C_R.

*Step 2***.** Assign initial values to the swarm by mapping the chaotic sequence, eq. (17). Investigate the position of particles. Estimate the fitness function value of the particles, *Fit*. Record the initial personal best position $\mathbf{P}_i$ and corresponding fitness function value $pbest_{\text{i}}$. Record the global best position $\mathbf{P}_g$ and corresponding fitness function value *gbest.* Set the initial value of the current iteration as $t = 0$.

*Step 3***.** Estimate whether the stop criteria are met. If the termination condition is reached, end the calculation. Record the estimated value. If not, continue with the next step:
– the tolerance ε is greater than the fitness function value of global best position, $\varepsilon > gbest$ and
– the iteration limit N_c is reached, $iter(t) > N_c$.

*Step 4***.** Calculate the diversity of the swarm according to eq. (16). According to eqs. (14) and (15), update the position of each particle $\mathbf{X}_i$. Evaluate the swarm and calculate the corresponding Fit_i.

Step 5. Update the personal best position $\mathbf{P}_i$ if current $pbesti$ of the i^{th} particle is inferior to the present fitness function value of the i^{th} particle.

Step 6. According to eqs. (18) and (19), estimate the trial vector $\mathbf{P}_{i,\text{tri}}$ for each particle, and evaluate the trial vector. Update target vector if the fitness function value of the target vector is inferior to that of the trial vector.

Step 7. Update the global best position $\mathbf{P}_g$ if the present personal best positions are better than the current *gbest*. Loop to *Step 3*.

Numerical simulation

The geometric structure of the fractal aggregates is investigated by minimizing the fitness function value fitting *Fit*, which is defined as the sum of the square residuals between the estimated signal and the measured signal. The *Fit* can be expressed:

$$Fit = \sum_{i=1}^{N_\theta} \left\{ \frac{I_X(\theta_i)_{\text{est}} - I_X(\theta_i)_{\text{mea}}}{I_X(\theta_i)_{\text{mea}}} \right\}^2, \quad I_X = I_{\text{a}} \ \text{or} \ I_{\text{f}} \tag{20}$$

where N_θ is the number of the measurement angles. The system control parameters used in the study are listed in tab. 1.

Table 1. System control parameters of the PSO algorithms

Parameters	N_s	N_c	ε	$v_{\max}$	C_1	C_2	d_{high}	d_{low}	μ	F	C_R
PSO	40	1000	$1.0\cdot10^{-8}$	10.0	2.0	2.0	–	–	–	–	–
ARPSO	40	1000	1.0E-8	10.0	–	–	0.25	$5.0\cdot10^{-6}$	–	–	–
IARPSO	40	1000	$1.0\cdot10^{-8}$	10.0	–	–	0.25	$5.0\cdot10^{-8}$	4.0	0.5	0.2

The algorithm used in the inverse problem has certain randomness. All the calculations are repeated $N = 30$ times as to reduce the impact of randomness. In the improved quantum particle swarm optimization algorithm, the reliability and feasibility are investigated, and the quality of inversion results is evaluated by studying the following parameters :

– The relative deviation ξ is defined as the sum of the deviation between the probability distribution estimated from the inverse calculation and the actual distribution of R_g in every subinterval:

$$\xi = \frac{\left\{ \sum_{i=1}^{N'} \left[f_{\text{est}}\left(\tilde{R}_{g,i}\right) - f_{\text{true}}\left(\tilde{R}_{g,i}\right) \right]^2 \right\}^{1/2}}{\left\{ \sum_{i=1}^{N'} \left[f_{\text{true}}\left(\tilde{R}_{g,i}\right) \right]^2 \right\}^{1/2}} \tag{21}$$

where N' is the number of subintervals that the size range $[R_{g,\min}, R_{g,\max}]$ is divided, $\tilde{R}_{g,i}$, $f_{\text{true}}(\tilde{R}_{g,i})$ and $f_{\text{est}}(\tilde{R}_{g,i})$ are the midpoint, the true distribution and the estimated distribution in the i^{th} subinterval $[R_{g,i}, R_{g,i+1}]$, respectively.

– Mathematical expressions of the relative error η and the standard deviation δ:

$$\eta X = \frac{\left| \bar{X}_{\text{est}} - X_{\text{real}} \right|}{X_{\text{real}}}, \quad X = D_{\text{f}}, R_g, R_{g,\text{av}} \ \text{ or } \ \sigma \tag{22}$$

$$\delta_X = \sqrt{\frac{1}{N} \sum_{i=1}^{N} \left(\bar{X}_{\text{est}} - X_{\text{est},i} \right)^2}, \quad \bar{X}_{\text{est}} = \frac{1}{N} \sum_{i=1}^{N} X_{\text{est},i}, \quad X = D_{\text{f}}, R_g, R_{g,\text{av}} \ \text{ or } \ \sigma \tag{23}$$

where $\bar{X}_{\text{est}}$ is the average values of the retrieval results and X_{real} – the real value of unsolved parameters.

Comparison of the convergence characteristics of different intelligent optimization algorithms

Compared with the PSO algorithm and the ARPSO algorithm, the performance of the IARPSO algorithm is studied in this paper. The R_g is considered to be constant to make the problem mathematically traceable. The real value of R_g is set as 80 and D_{f} is set as 1.8. The measurement angles are set θ = 5°, 15°, 25°, 35°. Table 2 shows the retrieval results using different inverse algorithm under different random measurement noises. It can be found that the retrieval accuracy of R_g is worse than that of D_{f}. The IARPSO algorithm converges much faster, and more accurate results can be obtained by the IARPSO algorithm than others even with random measurement noises. Thus, the IARPSO algorithm is selected in the following study.

Moreover, compared with the FLSM method, more satisfactory retrieval results can be obtained using the ALSM method even with 5% random measurement noise. The explanation can be found from fig. 3, which demonstrates the distributions of the fitness function values of the FLSM and ALSM methods. Obviously, the distributions of fitness function values of both methods present a canyon-like distribution, and the minimum value regions converge to a point near the real value, *i.e.* (D_{f}, R_g) = (1.8, 80). It indicates that the result is unique. When using the FLSM method, the fitness function value needs to reach $Fit = 10^{-14}$ to ensure inverse accuracy. While using the ALSM method, the fitness function value only needs to reach $Fit = 10^{-9}$. According to the theories of the inverse radiative problem and the intelligent optimization algorithm, if the fitness function needs to arrive at a lower value to ensure the inverse accuracy, the inverse algorithm is required to have better convergence accuracy and robustness. So, for a certain intelligent optimization algorithm, it is easy to obtain more accurate inverse results using the ALSM method than using the FLSM method even with random measurement noises.

Table 2. Results retrieved by different algorithms using different measurement methods

Inverse algorithms	Parameters	FLSM method		ALSM method	
		3%	5%	3%	5%
PSO	$\bar{D}_f$	$1.90 \pm 5.32\times10^{-1}$	$2.31 \pm 6.23\times10^{-1}$	$1.86 \pm 4.43\times10^{-1}$	$1.61 \pm 5.61\times10^{-1}$
	ηD_f	0.0556	0.2833	0.0333	0.1056
	$\bar{R}_g$	$101.32 \pm 2.24\times10^{1}$	$111.2 \pm 3.5\times10^{1}$	$85.34 \pm 1.3\times10^{1}$	$92.21 \pm 2.9\times10^{1}$
	ηR_g	0.2665	0.3900	0.0668	0.1526
	$\bar{t}(s)$	2276.23	2634.23	2217.16	2537.67
ARPSO	$\bar{D}_f$	$1.85 \pm 4.34\times10^{-1}$	$1.95 \pm 5.21\times10^{-1}$	$1.84 \pm 2.45\times10^{-1}$	$1.72 \pm 3.78\times10^{-1}$
	ηD_f	0.0278	0.0833	0.0222	0.0444
	$\bar{R}_g$	$95.81 \pm 1.47\times10^{1}$	$98.23 \pm 2.1\times10^{1}$	$77.23 \pm 9.1\times10^{0}$	$89.23 \pm 1.7\times10^{1}$
	ηR_g	0.1977	0.2279	0.0346	0.1154
	$\bar{t}(s)$	1965.13	2598.78	1847.41	2317.18
IARPSO	$\bar{D}_f$	$1.81 \pm 3.47\times10^{-1}$	$1.84 \pm 4.49\times10^{-1}$	$1.82 \pm 1.32\times10^{-1}$	$1.78 \pm 1.51\times10^{-1}$
	ηD_f	0.0056	0.0222	0.0111	0.0111
	$\bar{R}_g$	$89.89 \pm 2.35\times10^{0}$	$101.8 \pm 1.8\times10^{1}$	$79.72 \pm 3.4\times10^{0}$	$81.09 \pm 7.97\times10^{0}$
	ηR_g	0.1236	0.2725	0.0035	0.0136
	$\bar{t}(s)$	1765.66	2175.11	1546.78	1675.11

*The mean and standard deviation of the 30 times retrieval results are shown as the form of $x \pm y$ in the table

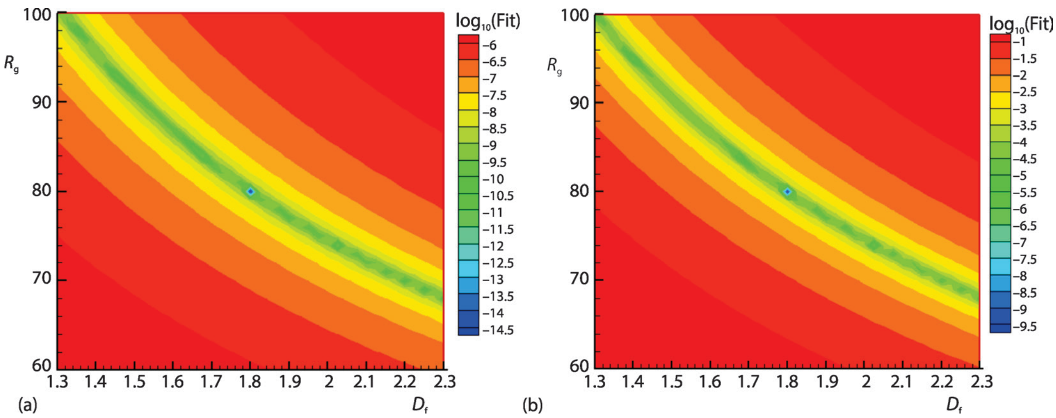

Figure 3. Distribution of fitness function values for different measurement methods with; (a) FLSM method and (b) ALSM method

Comparison of the retrieval results using different measurement angles

Generally, if the methods used in the measurement process and the inverse problem have been determined, the measurement signals selection has a significant impact on the retrieval accuracy, for the measurement signals obtained from different angles usually result in different retrieval accuracy. In this study, R_g is considered to obey *L-N* distribution. Thus, only the fractal dimension D_{f} and distribution characteristic parameters ($R_{g,\mathrm{av}}$, σ) of R_g needed to be investigated. The real values are set as (D_{f}, $R_{g,\mathrm{av}}$, σ) = (1.8, 80, 1.8). Table 3 lists the results re-

Table 3. Results retrieved by using different measurement methods and different measurement signals

Measurement methods	Measurement angles	Parameters	Noises		
			0%	1%	3%
FLSM	4 angels, θ = 5°, 15°, 25°, 35°	$\bar{D}_{\mathrm{f}}$	$1.75 \pm 6.85\times10^{-2}$	$1.71 \pm 4.04\times10^{-1}$	$1.63 \pm 5.67\times10^{-1}$
		ηD_{f}	0.0278	0.05	0.0944
		$\bar{R}_{g,\mathrm{av}}$	$105.22 \pm 1.33\times10^{1}$	$112.5 \pm 1.58\times10^{1}$	$118.2 \pm 2.23\times10^{1}$
		$\eta R_{g,\mathrm{av}}$	0.3153	0.4063	0.4775
		$\bar{\sigma}$	$2.05 \pm 9.84\times10^{-2}$	$2.12 \pm 4.29\times10^{-1}$	$2.22 \pm 4.67\times10^{-1}$
		$\eta\sigma$	0.1389	0.1778	0.2333
		ξ	0.279129	0.329144	0.363099
	6 angels, θ = 5°, 15°, 25°, 35°, 45°, 55°	$\bar{D}_{\mathrm{f}}$	$1.83 \pm 1.85\times10^{-2}$	$1.72 \pm 5.04\times10^{-1}$	$1.66 \pm 8.34\times10^{-1}$
		ηD_{f}	0.0167	0.0444	0.0778
		$\bar{R}_{g,\mathrm{av}}$	$95.72 \pm 5.56\times10^{0}$	$103.5 \pm 3.24\times10^{1}$	$112.8 \pm 2.34\times10^{1}$
		$\eta R_{g,\mathrm{av}}$	0.1965	0.2938	0.41
		$\bar{\sigma}$	$2.04 \pm 9.13\times10^{-2}$	$2.08 \pm 2.43\times10^{-1}$	$2.13 \pm 6.21\times10^{-1}$
		$\eta\sigma$	0.1333	0.1556	0.1833
		ξ	0.209301	0.268618	0.331068
ALSM	4 angels, θ = 5°, 15°, 25°, 35°	$\bar{D}_{\mathrm{f}}$	1.75±2.43×10-2	1.73±2.64×10-1	1.89±7.32×10-1
		ηD_{f}	0.0278	0.0389	0.05
		$\bar{R}_{g,\mathrm{av}}$	82.83±6.43×100	78.12±1.22×101	94.36±1.84×101
		$\eta R_{g,\mathrm{av}}$	0.0354	0.0235	0.1795
		$\bar{\sigma}$	2.04±8.23×10-2	2.06±4.21×10-1	2.09±6.65×10-1
		$\eta\sigma$	0.1333	0.1778	0.1611
		ξ	0.160792	0.192215	0.213211
	6 angels, θ = 5°, 15°, 25°, 35°, 45°, 55°	$\bar{D}_{\mathrm{f}}$	1.78±3.12×10-2	1.75±1.04×10-1	1.87±4.30×10-1
		ηD_{f}	0.0111	0.0278	0.0389
		$\bar{R}_{g,\mathrm{av}}$	80.22±4.72×100	84.61±9.8×100	89.97±1.63×101
		$\eta R_{g,\mathrm{av}}$	0.0028	0.0576	0.1246
		$\bar{\sigma}$	$1.96\pm3.84\times10^{-2}$	1.99±1.12×10-1	2.02±2.12×10-1
		$\eta\sigma$	0.0889	0.1056	0.1222
		ξ	0.119161	0.132916	0.167429

*The mean inverse results and standard deviation of the 30 times calculations are shown in the table trieved by the IARPSO algorithm using different measurement signals, and the retrieval curves are demonstrated in fig. 4. Compared with the results listed in tab. 2, it can be found that when R_g obeys the *L-N* distribution, the retrieval accuracy decreases even without measurement noise as the number of the parameters investigated increases. The retrieval result of R_g is still worse than that of D_f. Moreover, compared with the FLSM method, the ALSM method can get more accurate results. The explanation can also be found from the distributions of fitness function values showed in fig. 5. When using the FLSM method, the minimum value region of the fitness function is not unique, which means there are multi-value characteristics of retrieval results. When the minimum fitness function value, *i.e.* $10 \cdot 10^{-8}$ is reached, more than one couple of (D_f, $R_{g,\mathrm{av}}$, σ) existed. In the study of the fitness function values obtained by the ALSM method, the minimum value region is unique and only when the inverse algorithm converges to the region near the real value, *i.e.* (D_f, $R_{g,\mathrm{av}}$, σ) = (1.8, 80, 1.8), the corresponding fitness function value reaches the minimum value. Besides, when keeping the value of the interval between adjacent measurement angles unchanged, *i.e.* $\Delta\theta = 10°$, and increasing the number of the measurement angles, more satisfactory results can be obtained. The reason is that more measurement signals can supply more information about the particle system, which is benefit to weaken multi-valued characteristics of the retrieval results and improve the accuracy, especially random measurement noise is added.

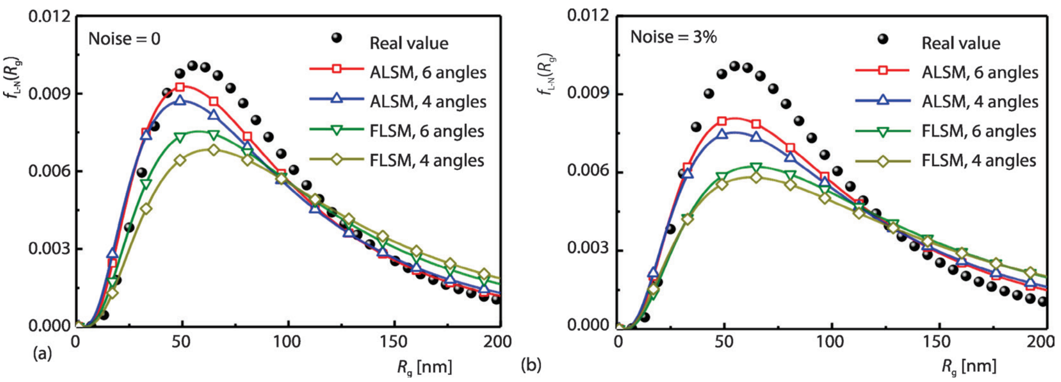

Figure 4. Retrieval curves of root mean square radius using different measurement methods

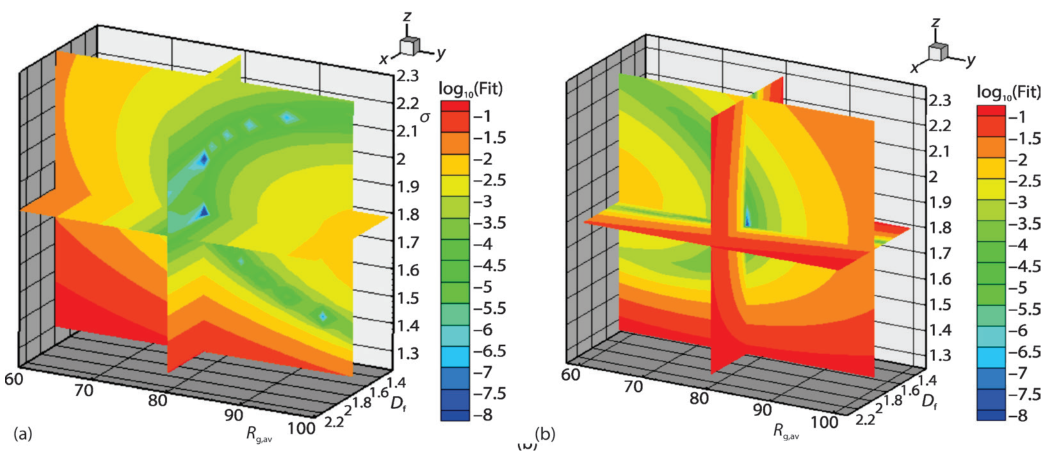

Figure 5. Distribution of fitness function values for different measurement methods with (D_f, $R_{g,\mathrm{av}}$, σ) = 1.8, 80, 1.8); (a) FLSM method and (b) ALSM method

The effect of different selections of measurement angles on the retrieval accuracy is also studied when the number of the measurement angles is determined. Table 4 lists the results retrieved by the ALSM method using different measurement angles, which are selected according to the arithmetic sequence. The corresponding retrieval curves are shown in fig. 6. It can be found that increasing the value of the interval between adjacent measurement angles will improve retrieval accuracy, especially for R_g.

Table 4. Results retrieved by using the measurement angles with different intervals

Measurement angles	Parameters	Noises 3%	Noises 5%
	$\bar{D}_f$	$1.68 \pm 5.34\times10^{-1}$	$1.61 \pm 6.45\times10^{-1}$
	ηD_f	0.0667	0.1056
	$\bar{R}_{g,av}$	$71.46 \pm 2.21\times10^{1}$	$61.10 \pm 3.23\times10^{1}$
	$\eta R_{g,av}$	0.1068	0.2363
	$\bar{\sigma}$	$1.65 \pm 4.32\times10^{-1}$	$2.24 \pm 5.68\times10^{-1}$
	$\eta\sigma$	0.0833	0.2444
	ξ	0.196851	0.468740
$\Delta\theta = 10°$, $\theta = 5°, 15°, 25°, 35°, 45°, 55°$	$\bar{D}_f$	$1.87 \pm 4.30\times10^{-1}$	$1.72 \pm 7.21\times10^{-1}$
	ηD_f	0.0389	0.0444
	$\bar{R}_{g,av}$	$89.97 \pm 1.63\times10^{1}$	$101.23 \pm 4.32\times10^{1}$
	$\eta R_{g,av}$	0.1246	0.2654
	$\bar{\sigma}$	$2.02 \pm 2.12\times10^{-1}$	$2.11 \pm 6.76\times10^{-1}$
	$\eta\sigma$	0.1222	0.1722
	ξ	0.167429	0.257426
$\Delta\theta = 15°$, $\theta = 5°, 20°, 35°, 50°, 65°, 80°$	$\bar{D}_f$	$1.75 \pm 2.32\times10^{-1}$	$1.86 \pm 6.23\times10^{-1}$
	ηD_f	0.0278	0.0333
	$\bar{R}_{g,av}$	$75.46 \pm 7.2\times10^{0}$	$88.19 \pm 3.65\times10^{1}$
	$\eta R_{g,av}$	0.0943	0.1024
	$\bar{\sigma}$	$1.88 \pm 1.98\times10^{-1}$	$2.02 \pm 4.43\times10^{-1}$
	$\eta\sigma$	0.1	0.1222
	ξ	0.110678	0.158716

*The mean inverse results and standard deviation of the 30 times calculations are shown in the table

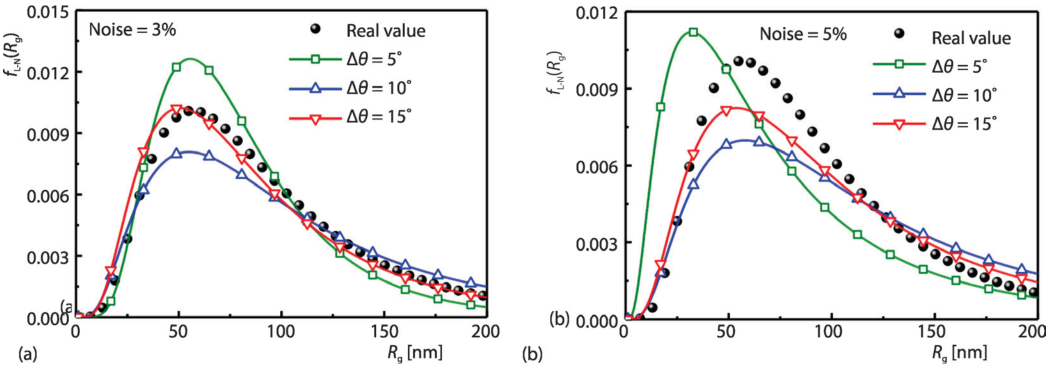

Figure 6. Retrieval curves of root mean square radius using the measurement angles with different intervals

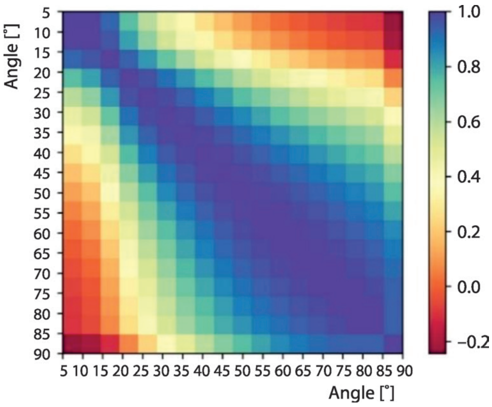

Figure 7. Correlation of ALSM signals between the measurement signals obtained different angles

The explanation can be found from fig. 7, which denotes the covariance matrix between the ALSM signals obtained from various measurement angles. The magnitude of the covariance value is shown by the color in each cell. According to the multivariate statistical analysis [17], the covariance $R_{i,j}$ is the measure of dependency between the measurement signals obtained at random angles:

$$R_{i,j} = Cov[I(\theta_i), I(\theta_j)],\ \ i,j = 1,...,Na \tag{24}$$

where Na is the number of measurement angles available, $I(\theta_i)$ is the an observation at a particular angle θ_i, which is usually p-dimensional multivariate, *e.g.* $I(\theta_i) = [I(\theta_i)_1, I(\theta_i)_2,... I(\theta_i)_p]$. If the measurement signals are independent of each other, the covariance is necessarily equal to zero. While there is high correlation between measurement signals, the covariance value will approach 1 or –1. For example, the covariance of $I(\theta_i)$ with itself is equal to 1. The theoretical covariances among all the measurement signals are put into matrix form:

$$\sum = \begin{bmatrix} R_{1,1} & & \cdots & & R_{Na,1} \\ R_{1,2} & \cdots & R_{i,j\text{-}1} & \cdots & \\ \vdots & R_{i-1,j} & R_{i,j} & R_{i+1,j} & \vdots \\ & \vdots & R_{i,j+1} & \vdots & \\ R_{1,Na} & & \cdots & & R_{Na,Na} \end{bmatrix} \quad i,j = 1,...,Na \tag{25}$$

It can be seen from fig. 7 that the area with the highest correlation is the diagonal line. The farther the measurement angles are, the smaller the correlation of the measurement signals is. The results imply that if the measurement angles close to each other, there will be less effective information carried by the measurement signals, which may reduce the benefits of the multi-angle measurement and decrease the accuracy of the inverse results. Therefore, to obtain more effective measurement information and improve the retrieval accuracy, it would be better to select the measurement angles with a larger interval.

Conclusions

Based on the IARPSO algorithm, the present manuscript investigates the robustness and reliability of the ALSM and the FLSM method in retrieving the fractal aggregates' geometric feature parameters. Moreover, the effect of the signals obtained from different measurement angles on the retrieval accuracy are also studied. The research conclusions are of this paper.

- The IARPSO algorithm can obtain more accurate results with less convergence time than the PSO algorithm and ARPSO algorithm even with random measurement noises in retrieving the fractal aggregates' geometric feature parameters.
- Compared with the FLSM method, the ALSM method has higher convergence accuracy and better robustness, because the distribution of the fitness function value obtained by the latter method is more conducive to avoid multi-value characteristic of retrieval results and improve the retrieval accuracy.

- When the number of measurement angles is constant, the inversion results will become better as the interval between adjacent measurement angles increases. The reason is that the increase of the interval between the measurement angles will make the corresponding measurement signals more independent of each other. This is beneficial to obtain more effective measurement information.

In conclusion, all numerical studies show that the IARPSO algorithm combined with the ALSM method is a reliable and satisfactory methodology to reconstruct the geometrical structure of fractal aggregates. Moreover, to improve retrieval accuracy, adding the number of measurement angles or the value of the interval between adjacent measurement angles is an effective method.

Acknowledgment

The supports of this work by the National Natural Science Foundation of China (No. 51806103, 91841302), Natural Science Foundation of Jiangsu Province (No: BK20170800), and Defense Industrial Technology Development Program (No. JCKY2018605B006), and they are gratefully acknowledged. A very special acknowledgment is made to the editors and referees who make important comments to improve this paper.

Nomenclature

a – mean radius of the monomer, [nm]
$C_{\mathrm{abs},\lambda,i}^{agg}$ – absorption cross-section of aggregates, [m^2]
$C_{\mathrm{sca},\lambda,i}^{agg}$ – scattering cross-section of aggregates, [m^2]
C_R – crossover constant, [–]
D – diameter of particles, [μm]
D_f – fractal dimension of aggregates, [–]
F – objective function value, [–]
$f(D)$ – volume frequency distribution, [–]
Fit – fitness function value, [–]
$G(kR_g)$ – generalization function, [–]
I – radiative intensity, [Wm^{2}sr)]
I_0 – total intensity of incident laser, [Wm^{2}sr)]
$I(\theta)$ – angular light-scattering intensity at the angle θ, [Wm^{2}sr)]
k – wave number in the vacuum, [–]
k_f – fractal prefactor of aggregates, [–]
L – geometrical thickness of the measurement sample, [m]
m – complex refractive index of monomers, [–]
N – dimensionality of the problem, [–]
N_D – total number of particles, [–]
$\mathbf{P}_g$ – global best position, [–]
$\mathbf{P}_i$ – best position of the i^{th} particle, [–]
p_{ij} – j^{th} value of the ith particle, [–]
Q_ext – extinction efficiency, [–]
R_g – root mean square radius, [nm]
$R_{g,\mathrm{av}}$ – characteristic radius in the *L-N* distribution function, [nm]
$R_{i,j}$ – covariance between different measurement signals, [–]
$|S|$ – Swarm size, [–]
$S(qRg)$ – aggregate structure factor, [–]
t – time or iteration in IARPSO algorithm, [s]
$\mathbf{V}_i$ – candidate position of food source, [–]
$\mathbf{X}_i$ – the position of food source, [–]

Greek symbols

α_λ – spectral absorption coefficient, [m–1]
δ – standard deviation of the inverse results, [–]
ε – tolerance, [–]
η – relative error of the inverse results, [–]
θ – light scattering angle, [–]
λ – wavelength of laser, [μm]
ξ – relative deviation between the estimated distribution and real distribution of R_g, [–]
σ – narrowness index in the L-N distribution function, [–]
σ_λ – spectral scattering coefficient, [m^{-1}]
$\Phi_\lambda(\vec{s}_i, \vec{s})$ – scattering phase function of aggregates, [–]
Ω – solid angle in solving the RTE by the FVM, [–]
ω – inertia weight, [–]

Subscripts

est – estimated value, [–]
ext – extinction efficiency, [–]
high – high limit of the search space, [–]
low – low limit of the search space, [–]
max – the maximum value, [–]
mea – measurement value, [–]
min – minimum value, [–]
true – true value, [–]
obj – objective function, [–]

References

[1] Modest, M. F., The Weighted-Sum-of-Gray-Gases Model for Arbitrary Solution Methods in Radiative Transfer, *Asme Transactions Journal of Heat Transfer*, *113* (1991), 3, pp. 650-656

[2] Mishchenko, M. I., *et al*., *Scattering, Absorption, and Emission of Light by Cmall Particles*, Cambridge University Press, Cambridge, Mass., USA, 2002

[3] Liu, L., *et al*., A s Study of Radiative Properties of Fractal Soot Aggregates Using the Superposition T-Matrix Method, *Journal of Quantitative Spectroscopy and Radiative Transfer*, *109* (2008), 15, pp. 2656-2663

[4] He, Z. Z., *et al*., Investigation on the Effect of Fractal Soot Aggregation on Radiative Transfer in Homogeneous Gas-Soot Mixture Using Full-Spectrum k-Distribution Method, *Journal of Thermal Science and Technology*, *14* (2019), 1, pp. JTST0001-JTST0001

[5] Kholghy, M. R., *et al.*, Comparison of Multiple Diagnostic Techniques to Study Soot Formation and Morphology in a Diffusion Flame, *Combustion and Flame*, *176* (2017), Feb., pp. 567-583

[6] Gwaze, P., *et al.*, Comparison of Three Methods of Fractal Analysis Applied to Soot Aggregates from Wood Combustion, *Journal of Aerosol Science*, *37* (2006), 7, pp. 820-838

[7] Bescond, A., *et al*., Automated Determination of Aggregate Primary Particle Size Distribution by TEM Image Analysis: Application Soot, *Aerosol Science and Technology*, *48* (2014), 8, pp. 831-841

[8] Caumontprim, C., *et al*., Measurement of Aggregates' Size Distribution by Angular Light Scattering, *Journal of Quantitative Spectroscopy and Radiative Transfer*, *126* (2013), S1, pp. S140-S149

[9] Sorensen, C., Light Scattering by Fractal Aggregates: A Review, *Aerosol Science and Technology*, *35* (2001), 2, pp. 648-687

[10] Steinmetz, S. A., *et al*., Soot Particle Size Measurements in Ethylene Diffusion Flames at Elevated Pressures, *Combustion and Flame*, *169* (2016), July, pp. 85-93

[11] He, Z. Z., *et al*., Application of the Steady-State and Unsteady-State Lasers in Reconstructing the Geometrical Characteristic Parameters of Soot Fractal Aggregates, *Optik-International Journal for Light and Electron Optics*, *202* (2020), 163720

[12] Qi, H., *et al*., Inverse Radiation Analysis of a 1-D Participating Slab by Stochastic Particle Swarm Optimizer Algorithm, *International Journal of Thermal Sciences*, *46* (2007), *7*, pp. 649-661

[13] Riget, J., Vesterstrom, J. S., A Diversity-Guided Particle Swarm Optimizer-the ARPSO, Report No. 2002-02, University of Aarhus, Aarhus, Denmark, 2002

[14] Qi, H., *et al*., Inversion of Particle Size Distribution by Spectral Extinction Technique Using the Attractive and Repulsive Particle Swarm Optimization Algorithm, *Thermal Science*, *19* (2015), 6, pp. 2151-2160

[15] Ren, Y. T., *et al.*, Simultaneous Retrieval of the Complex Refractive Index and Particle Size Distribution, *Opt. Express*, *23* (2015), 15, pp. 19328-19337

[16] Zhang, B., *et al*., Solving Inverse Problems of Radiative Heat Transfer and Phase Change in Semitransparent Medium by Using Improved Quantum Particle Swarm Optimization, *International Journal of Heat and Mass Transfer*, *85* (2015), June, pp. 300-310

[17] Hardle, W. K., Simar, L., Applied Multivariate Statistical Analysis, *Technometrics*, *47* (2005), 4, pp. 517-517

Paper submitted: February 14, 2020
Paper revised: June 29, 2020
Paper accepted: July 2, 2020